

Band structure of CuMnAs probed by optical and photoemission spectroscopy

M. Veis,¹ J. Minár,² G. Steciuk,³ L. Palatinus,³ C. Rinaldi,⁴ M. Cantoni,⁴ D. Kriegner,^{3,1} K.K. Tikuišis,¹ J. Hamrle,¹ M. Zahradník,¹ R. Antoš,¹ J. Železný,³ L. Šmejkal,³ P. Wadley,⁵ R.P. Champion,⁵ C. Frontera,⁶ K. Uhlířová,¹ T. Duchoň,⁷ P. Kužel,⁸ V. Novák,³ T. Jungwirth,^{3,5} and K. Výborný³

¹Charles University, Faculty of Mathematics and Physics, Ke Karlovu 5, Praha 2, Czech Republic

²New Technologies-Research Center University of West Bohemia, Plzeň, Czech Republic

³Institute of Physics, Academy of Science of the Czech Republic, Cukrovarnická 10, Praha 6, Czech Republic

⁴Department of Physics, Politecnico di Milano, via G. Colombo 81, 20133, Milano, Italy

⁵School of Physics and Astronomy, University of Nottingham, Nottingham NG7 2RD, United Kingdom

⁶Institut de Ciència de Materials de Barcelona (ICMAB-CSIC),

Campus Universitari de Bellaterra, Cerdanyola del Vallès, 08193 Spain

⁷Charles University, Faculty of Mathematics and Physics,

Department of Surface and Plasma Science, V Holešovičkách 2, 18000 Praha 8, Czech Republic

⁸Institute of Physics, Academy of Science of the Czech Republic, Na Slovance 1999/2, Praha 8, Czech Republic

(Dated: Dec01, 2017 version + SI)

Tetragonal phase of CuMnAs progressively appears as one of the key materials for antiferromagnetic spintronics due to efficient current-induced spin-orbit torques whose existence can be directly inferred from crystal symmetry. Theoretical understanding of spintronic phenomena in this material, however, relies on the detailed knowledge of electronic structure (band structure and corresponding wave functions) which has so far been tested only to a limited extent. We show that AC permittivity (obtained from ellipsometry) and UV photoelectron spectra agree with density functional calculations. Together with the x-ray diffraction and precession electron diffraction tomography, our analysis confirms recent theoretical claim [Phys.Rev.B 96, 094406 (2017)] that copper atoms occupy lattice positions in the basal plane of the tetragonal unit cell.

Magnetic moments in antiferromagnets have been notoriously difficult to manipulate. With the exception of materials having low Néel temperature and small magnetic anisotropy, very strong magnetic fields must be applied. Such fields would be too strong to be of any practical use and, moreover, they can never be applied as locally as electric pulses. Recently, an alternative manipulation mechanism has been proposed¹ which relies on current-induced spin-orbit torques (SOTs) acting in the bulk of the antiferromagnetic material. They result from a build-up of staggered spin polarisation (i.e. the one which alternates sign on two magnetic sublattices) in response to an applied uniform electric current; such polarisation can be calculated in the framework of linear response to electric field.^{2,3} A prediction of sizable SOT in CuMnAs has soon been experimentally confirmed⁴ and prototype memories where the writing is done using SOT have been demonstrated.⁵ Devices based on thin films of CuMnAs thus claim a prominent role within the fast developing field of antiferromagnetic spintronics.^{6,7}

Quantitative modelling of SOT (and many other material-specific quantities) relies on a detailed knowledge of the electronic structure.⁸ While well-established ab initio methods have been used for this purpose, little effort has so far been dedicated to validating the band structure in terms of comparing calculated and measured spectral properties.⁹ We fill this gap by exploring the complex AC permittivity in the optical range and photoemission spectroscopy in the UV range (UPS) and comparing them to density functional theory (DFT) calculations. We find a good agreement between the experimental data and the calculated properties provided the elec-

tronic correlations are treated beyond DFT, using Hubbard model characterised by an on-site repulsion U on Mn $3d$ orbitals. Moreover, we demonstrate that the AC permittivity in the optical range can be used to discern different phases of CuMnAs. Focusing on the tetragonal phase of CuMnAs,¹⁰ we corroborate analysis of our spectral measurements by precession electron diffraction tomography (PEDT), which points to a phase recently claimed to have the lowest theoretically calculated total energy.¹¹

The studied thin films of CuMnAs were prepared by molecular beam epitaxy (MBE; we followed procedures described in Ref. 10). We performed the standard x-ray diffraction (XRD) structural characterisation and PEDT. Ellipsometry was carried out on a nominally 20 nm thick layer, while PEDT was applied to 150 nm thick layers, both grown on a GaP(001) substrate. Photoemission spectra in the UV range (UPS) were obtained for a 130 nm thick sample grown on a GaAs(001) substrate.

Both XRD and PEDT confirm the tetragonal crystal structure shown in Fig. 1 with space group $P4/nmm$. Regarding the occupancy of lattice sites labelled S^1 , S^2 and S^3 in the Figure, neither x-ray nor electron diffraction are very efficient in distinguishing manganese and copper atoms because of their similar scattering powers; the latter method, however, does provide some advantage over the former one as we show below. In this work, we consider theoretically two tetragonal phases which are defined as follows: the first structure has copper atoms at the basal positions S^1 (Wyckoff position $2a$) and As/Mn at S^2/S^3 (Wyckoff position $2c$). We will refer to this as the reference tetragonal phase (RTP). The second, in-

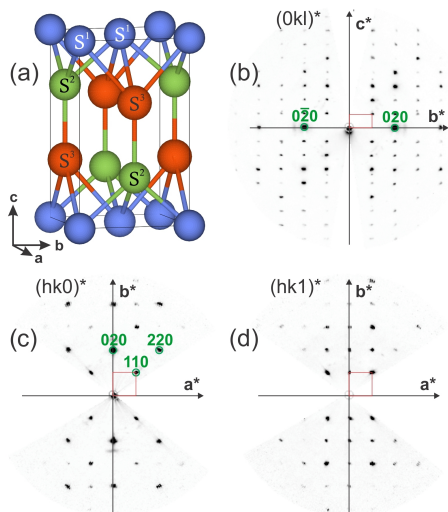


FIG. 1. (a) Structure of the tetragonal phase of CuMnAs. In RTP, Cu/As/Mn atoms occupy the sites $S^1/S^2/S^3$. In the inverted phase, Cu and Mn atoms are swapped. (b-d) Electron diffraction (PEDT) patterns: $(0kl)^*$, $(hk0)^*$ and $(hk1)^*$ sections of the reciprocal space reconstructed from PEDT data (PETS program¹³). The conditions $h+k = 2n$ on $hk0$, $h = 2n$ on $h00$ and $k = 2n$ on $0k0$ are characteristic of the n glide.

verted structure is obtained by swapping Mn and Cu so that the basal positions S^1 are occupied by manganese. Regarding magnetic structure of the latter phase, we only consider the case of antiferromagnetic ordering within the basal plane where the unit cell contains six atoms.

Using XRD, we find lattice constants differing by less than 1% for samples grown on GaP and GaAs (e.g. $a = 0.3853$ nm and $a = 0.3820$ nm at room temperature, respectively). For the purpose of effects considered in this work, such differences lead to negligible changes in observed spectra, which renders, within the scope of this article, all our thin film samples interchangeable. Further details about x-ray characterisation can be found in the Supplementary information¹² (Sec. I) and we now turn our attention to the electron diffraction analysis.

For PEDT characterisation, a cross section of the CuMnAs/GaP(001) thin film was prepared by mechanic polishing followed by ion milling. Four PEDT data sets were recorded on several parts of the film using a Philips CM120 electron transmission microscope ($V_{acc} = 120$ kV, LaB₆) with the precession device Nanomegas Digistar and a side-mounted CCD camera Olympus Veleta with 14bit dynamic range. The precession angle and the tilt step of the goniometer were both set to 1 degree. The data were analysed using the computer programs PETS¹³ and JANA2006.¹⁴

Tetragonal structure as shown in Fig. 1(a) was confirmed by the PEDT data. Extinction conditions observed on the sections of the reciprocal space shown in Figs. 1(b-d) are compatible with the space group $P4/nmm$. RTP was used as a starting structure and refined from the PEDT data using the dynamical the-

ory of diffraction ("dynamical refinement") according to Refs. 17 and 18. All four PEDT data sets were combined in order to increase the statistics of the refinement and the coverage of the reciprocal space. Results of the refinement are summarised in Table I. We measured almost five thousand reflections in all data sets (N_{all}) and found N_{obs} reflections with a significant intensity. Among model parameters, there are seven structural parameters (two z/c parameters, three displacement parameters and two occupancy factors), an average thickness of the analysed area for each of the four datasets and one scaling parameter per each experimental diffraction pattern giving in total $N_{param} \ll N_{obs}$ optimised parameters. Note that data-to-parameter ratio $N_{all}/N_{param} > 10$ is required for a reliable structure determination. The quality of the fit is demonstrated by the R -value¹⁹ of 10.46 and only slightly larger weighted R -value. For atomic positions z/c , we obtain values in a good agreement with the corresponding values inferred from x-ray analysis.¹² The occupancy of S^3 is found significantly different from one suggesting that our samples are copper-rich.

The key added value of PEDT in the context of this study is the ability to better distinguish RTP from the inverted structure, and to this end, the isotropic displacement parameters $U_{iso}(S^1)$ and $U_{iso}(S^3)$ (also known as ADP) are the most sensitive indicators. If atomic types are correctly assigned to individual atomic positions, their values should be approximately equal. For the S^1 and S^3 sites in Fig. 1, the ADPs in the RTP model do have similar values, consistent with previous studies.^{15,16} However, they change unfavourably for the inverted tetragonal phase: the ADP drops (increases) by about 65% for the S^1 (S^3) site, respectively. This result is consistent with the higher electron atomic scattering amplitude of Cu (f_{Cu}^B) relative to Mn (f_{Mn}^B). In other words, RTP seems more consistent with the electron diffraction data. Note that also the R -value in Tab. I for the inverted structure is appreciably larger than for RTP.

A Mueller matrix ellipsometer JA Woollam RC2 was employed to acquire experimental spectra of ellipsometric parameters Ψ and Δ . To ensure a sufficiently large ensemble of experimental data necessary for fitting, spectra were measured at several angles of incidence ($55^\circ, 60^\circ, 65^\circ, 70^\circ$). The experimental data were fitted using the Woollam CompleteEase software starting with a model structure of nominally 20 nm thick CuMnAs layer on GaP substrate and a surface oxide layer was accounted for, which naturally occurs when the sample is exposed to air (see Sec. II of Supplementary information¹² for details). Optical constants of GaP were taken from literature,²¹ while the permittivity of CuMnAs was parametrised by a combination of Drude, Tauc-Lorentz and three Lorentz functions. All parameters were fitted together with the layer thickness (l_{CuMnAs}) and surface roughness. The resulting $l_{CuMnAs} = 22.6$ nm along with a negligible surface roughness confirm the high level of sample growth control. Also, the mean square error (MSE) was lower than 1, im-

TABLE I. Crystallographic and dynamical refinement parameters of the RTP and the inverted tetragonal phases, both of $P4/nmm$ (No. 129) space group. For RTP: Cu (S^1) occupies the Wyckoff position 2a ($\frac{1}{2}, \frac{1}{2}, 0$), Mn (S^3) and As (S^2) occupy positions 2c ($0, \frac{1}{2}, z$). In the inverted tetragonal phase S^1 =Mn and S^3 =Cu.

Structural parameters:		occupancies			ADPs (iso.)[\AA^2]			
	z/c	S^1	S^2	S^3	S^1	S^2	S^3	
RTP:	0.2627(2)	0.6628(2)	0.995(8)~1	1	0.869(7)	0.0147(4)	0.0121(3)	0.0123(4)
inverted:	0.2627(2)	0.6624(2)	0.870(6)	1	0.949(8)	0.0052(4)	0.0124(3)	0.0205(5)
Refinement parameters:								
RTP:	$N_{param.}=338$;	$N_{obs/all.}=3768/4189$;	$R_{obs}=10.15$;	$wR_{all}=11.86$				
inverted:	$N_{param.}=338$;	$N_{obs/all.}=3767/4190$;	$R_{obs}=10.68$;	$wR_{all}=12.51$				

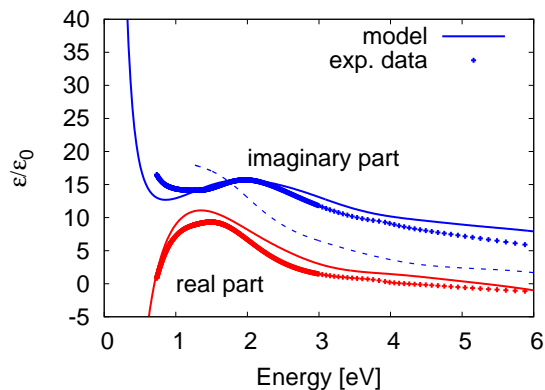


FIG. 2. AC permittivity of CuMnAs thin film determined by ellipsometry (for comparison, $\text{Im } \epsilon/\epsilon_0$ for orthorhombic bulk CuMnAs is shown by the dotted line; see Supplementary information,¹² Sec. III). The GGA+U model uses $U = 1.7$ eV and $\Gamma = 0.7$ eV for the interband part and $\hbar\omega_p = 3.26$ eV and $\hbar/2\tau = 120$ meV for the intraband contribution.

plying a rather robust fit whose result is shown in Fig. 2 as experimental data.

Our DFT+U calculations²⁰ for tetragonal CuMnAs ($a = 0.3853$ nm, $c = 0.6276$ nm) based on generalised gradient approximation (GGA) with scalar-relativistic correction come quite close to the experimental data (Fig. 2), provided relatively large interband broadening ($\Gamma = 0.7$ eV) is used. Such value is not unprecedented²² although still significantly larger than $\hbar/2\tau$ implied by Drude-formula relaxation time τ obtained from measured DC conductivity. This said, one should be reminded that the intra- and interband relaxation times are not required to be the same so that parameters used for the model in Fig. 2 are still plausible. To estimate τ , we used (apart from the experimental resistivity¹⁰) the ab-initio calculated plasma frequency ω_p . The model data plotted in Fig. 2 include also the intraband contribution (Drude peak). From this point on, we will only be discussing the imaginary part of permittivity since the Kramers-

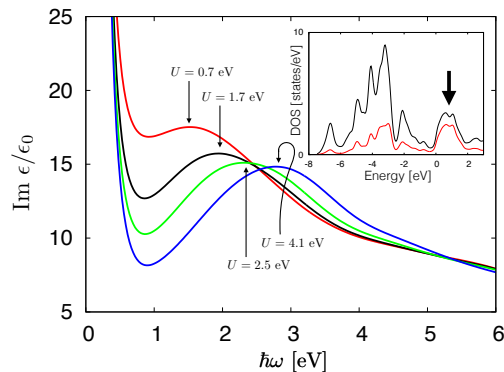


FIG. 3. Imaginary part of relative permittivity calculated for several values of U . The peak shifts blue with increasing U , the arrows indicate the position of the maximum. *Inset*: density of states per spin (and Mn-partial density of states shown in red) with a Mn-dominated peak just above the Fermi level (taken as $E = 0$).

Kronig-related real part bears no additional information.

Accounting for electron correlations turns out to be essential. We use GGA+U with double-counting corrections to the DFT part treated in the fully localised limit²³ (FLL) and find the peak in imaginary part of the permittivity blue-shifting with increasing value of U (see Fig. 3). Its experimentally determined position ($\hbar\omega \approx 2$ eV) is recovered for $U = 1.7$ eV and on the theoretical side, the peak stems from unoccupied Mn states (indicated by an arrow in the inset of Fig. 3). In Fig. 4, the corresponding band structure is shown. We now also briefly discuss the effect of the parameter²³ $J > 0$. It causes the peak in $\text{Im } \epsilon/\epsilon_0$ to shift to lower energies (in agreement with replacing U and J by $U_{\text{eff}} = U - J$ and $J = 0$), and also it adds some additional structure to the peak. The large interband broadening, however, renders such effects unobservable. Based on ellipsometry data, values of $U - J \approx 2$ eV therefore seem to give the best results.

Photoemission spectra and also inverse photoemission spectra (IPES) were measured for CuMnAs thin layers covered originally (after growth) by an arsenic cap. This

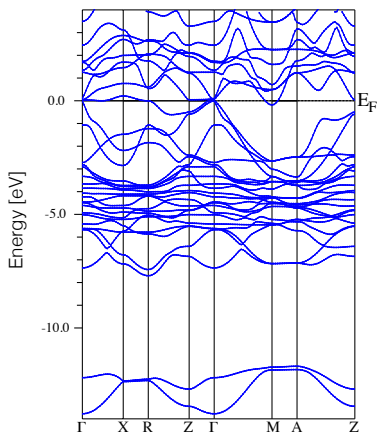


FIG. 4. Based on comparison between ellipsometry and GGA+ U calculations,²⁰ this band structure ($U = 1.7$ eV) seems to describe well CuMnAs in tetragonal phase.

protective layer was removed by Ar ion milling in the UHV environment for UPS and IPES.²⁴ The cleanliness of the surface was checked in-situ by X-ray Photoemission Spectroscopy (XPS): the disappearance of core-level peaks O 1s and C 1s indicates that the surface is clean (the residual contamination is well below 1% of surface coverage). The UPS spectrum was recorded using a He lamp as excitation source ($\text{HeI-}\alpha = 21.2$ eV) and a hemispherical energy analyser Phoibos 150 (SPECSTM), yielding an acceptance angle of $\sim 6^\circ$ and a field view of 1.4 mm². The UPS spectrum of CuMnAs is shown in Fig. 5 by black squares. Results of the investigation of empty states above the Fermi level by IPES is shown only in the Supplementary Information¹² (Section IV). As a matter of fact, the calculated DOS above the Fermi level is less sensitive to variations of U and, moreover, fine details cannot be accessed by IPES because of the large experimental broadening²⁶ characteristic of these spectra.

Photoemission spectroscopies access the electronic structure associated with top ≈ 1 nm of the thin layer.²⁵ In the simplest approximation, the measured angle-integrated UPS and IPES should reflect rather directly the DOS. This approximation works reasonably well in the high energy regime (XPS) and led²⁷ to a larger estimate of U around 4.5 eV. However, this approach ignores the influence of specific matrix elements that, in general, introduce an energy- and element-dependent weight to DOS. Also, in the regime of low photon energies (as measured here), additional aspects may have a very pronounced impact on the angle-integrated photoemission spectra, for example final states as well as surface effects.

Here we used the recently developed full spin-density matrix formulation for the photocurrent^{28,30} (see details in Supplementary information¹²) within the relativistic Korringa-Kohn-Rostoker Green function method. This method is implemented in the SPR-KKR program package.²⁹ Regarding the value of U , we arrive at a somewhat different conclusion than what was made in Ref. 27.

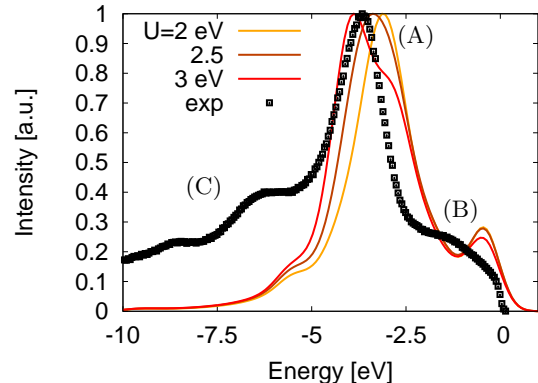


FIG. 5. Experimental angle-integrated photoemission (UPS, black squares) compared to the corresponding one-step model of photoemission. Theoretical data are shown for three values of U , labelled features are described in the text.

Nevertheless, the DOS shown in the inset of Fig. 3 still provides a good means for interpreting, on an elementary level, both the calculated and the measured spectra. They are dominated by the Mn states located at ≈ 1 eV and -4 eV (with respect to the Fermi level), the latter having a significant admixture of Cu states. The peak at ≈ -2 eV with dominantly Cu character is not visible in the UPS spectra, being probably hidden in the main peak of the measured data. The three main features in experimental spectra are labelled by capital letters in Fig. 5. It turns out that the main strong peak (A) serves as the best test for calculated spectra and their dependence on the value of U . As this value increases, the peak blue-shifts and a match with the experiment occurs between 2.5 eV and 3 eV (see Fig. 5; note, however, that the shoulder which develops in model calculations for $U = 3$ eV is absent in experimental data suggesting the plausibility of lower values of U). Both this feature and (C) which is also clearly visible in the model calculations, can be back tracked to the Mn d -states which are shifted to higher binding energies when U increases. The broad peak (B) located close to the Fermi level shows a strong surface character. We confirmed this theoretically by modifying the surface barrier (see Sec. IV. in Supplementary information¹²). Given that the surface was probably damaged by ion milling used to remove the cap, only little information about the bulk electronic structure can be extracted from this part of UPS. The level of agreement between UPS data and DFT+ U calculations suggests that aforementioned $U - J \approx 2$ eV is an acceptable value for the band structure calculations (using the particular method of Ref. 20).

In conclusion, we presented optical spectra of the complex permittivity and photoemission spectra in the UV regime of MBE-grown thin layers of CuMnAs, which crystallise in the tetragonal structure, and demonstrated

a good level of agreement with the DFT+U calculations. Together with the dynamically refined precession electron diffraction tomography, this agreement strongly suggests that copper occupies the basal positions of the structure (S^1 in Fig. 1) and this confirms the conclusions of the recent theoretical study of Máca et al. [11].

We acknowledge discussions with R. Bertacco and support from National Grid Infrastructure MetaCentrum provided under the programme "Projects of Large

Research, Development, and Innovations Infrastructures" (CESNET LM2015042); Grant Agency of the Czech Republic under No. 15-13436S; CEDAMNF (CZ.02.1.01/0.0/0.0/15_003/0000358) of the Czech ministry of education (MŠMT); Cariplo Foundation, grant No. 2013-0726 (MAGISTER); Spanish MINECO under MAT2015-67593-P project and the 'Severo Ochoa' Programme (SEV-2015-0496); EU FET Open RIA Grant no. 766566.

-
- ¹ J. Železný et al., Phys. Rev. Lett. 113, 157201 (2014).
² V.M. Edelstein, Sol. St. Comm. 73, 233 (1990).
³ B.A. Bernevig and O. Vafek, Phys. Rev. B 72, 033203 (2005).
⁴ P. Wadley et al., Science 351, 587 (2016).
⁵ K. Olejník et al., Nat. Comm. 8:15434 (2017).
⁶ V. Baltz et al., Rev. Mod. Phys. (to appear in 2017), arXiv1606.04284
⁷ T. Jungwirth et al., Nat. Nanotech. 11, 231 (2016).
⁸ Hang Li et al., Phys. Rev. B 91, 134402 (2015).
⁹ A notable exception is the calculation of magnetic linear dichroism in the x-ray range (see Fig. S2 in the Supporting material of Ref. 4). While these measurements allow for the identification of magnetic moment orientation, the spectral form is not in complete agreement with model calculations.
¹⁰ P. Wadley et al., Nat. Comm. 4:2322 (2013).
¹¹ F. Máca et al., Phys. Rev. B 96, 094406 (2017).
¹² Supplementary information to this article.
¹³ L. Palatinus, PETS - program for analysis of electron diffraction data. Institute of Physics of the AS CR, Prague, Czech Rep. (2011).
¹⁴ V. Petříček, M. Dušek, L. Palatinus, Z. Kristallogr. 229, 345 (2014).
¹⁵ P. Wadley et al., J. Appl. Cryst. 46, 1749 (2013).
¹⁶ A.N. Nateprov et al., Surf. Eng. and Appl. Electrochem. 47, 540 (2011).
¹⁷ L. Palatinus et al., Acta Crystallogr. A 71, 235 (2015).
¹⁸ L. Palatinus et al., Acta Crystallogr. B 71, 740 (2015).
¹⁹ The R -factor describes the average match between measured (F_{obs}) and calculated (F_{calc}) diffraction peak intensity: $R = 100 \cdot \sum_i (|F_{obs}| - |F_{calc}|) / \sum_i |F_{obs}|$.
²⁰ P. Blaha, K. Schwarz, G. K. H. Madsen, D. Kvasnicka and J. Luitz, *WIEN2k, An Augmented Plane Wave + Local Orbitals Program for Calculating Crystal Properties* (Karlheinz Schwarz, Techn. Universität Wien, Austria), 2001. ISBN 3-9501031-1-2
²¹ D.E. Aspnes and A.A. Studna, Phys. Rev. B 27, 985 (1983).
²² T. Berlijn et al., Phys. Rev. Lett. 106, 077005 (2011).
²³ V.I. Anisimov et al., Phys. Rev. B 48, 16929 (1993).
²⁴ R. Bertacco et al., App. Surf. Sci. 252, 1754 (2005).
²⁵ S. Hüfner, Photoelectron Spectroscopy, Springer (2003).
²⁶ M. Cantoni et al., Review of Scientific Instruments 70, 3572 (1999).
²⁷ J. Železný, PhD. thesis (MFF UK, Praha, 2016). DOI: 10.13140/RG.2.1.4579.4800
²⁸ J Braun et al., New J Phys 16, 015005 (2014).
²⁹ H. Ebert et al., Rep. Prog. Phys. 74, 096501 (2011). The Munich SPR-KKR package, version 7.7, <http://olymp.cup.uni-muenchen.de/ak/ebert/SPRKKR>
³⁰ J.B. Pendry, Surf. Sci. 57, 679 (1976).
³¹ P. Wadley et al., J. Appl. Cryst. 46, 1749 (2013).
³² U. Pietsch, V. Holý and T. Baumbach: High-Resolution X-Ray Scattering From Thin Films to Lateral Nanostructures, Springer 2004.
³³ J.B. Pendry, Low energy electron diffraction, Academic Press (1974).
³⁴ J Braun et al., New J Phys 16, 015005 (2014).
³⁵ G. Malmström and J. Rundgren, Computer Physics Comm. 19, 263 (1980).
³⁶ A. Nuber et al., Phys. Rev. B 83, 165401 (2011).
³⁷ M. Cantoni et al., Review of Scientific Instruments 70, 3572 (1999).
³⁸ K. Uhlířová et al., Journal of Alloys and Compounds 650, 224 (2015).
³⁹ Eve Emmanouilidou et al., arXiv1708.09340 (2017).

SUPPLEMENTARY INFORMATION \equiv REF. 12

I. X-RAY CHARACTERISATION

X-ray scattering and diffraction measurements were used to check the thin-film thickness and the tetragonal structure in Fig. 1 of the main text. The obtained parameters, described in detail below, are summarised in Tab. II here, and can be compared to values from Tab. I in the main text. We first describe the X-ray reflectivity analysis which yields the film thickness and roughness of the sample which we compare to the analysis of ellipsometric measurements. After that we turn to the structural characterization complementary to the PEDT data presented in the main text.

A. X-ray reflectivity analysis of the film thickness

X-ray reflectometry (XRR) was recorded with a Rigaku Smartlab rotating anode system using monochromatic X-ray photons with $\text{CuK}_{\alpha 1}$ wavelength. Since the refractive index of materials is below unity total external reflection occurs under small incidence angles. Above the critical angle where the X-rays penetrate the film material, Kiessig fringes due to the interference of X-rays reflected at the top and bottom interface of the thin film correspond to the film thickness and can be modeled by the Parrat formalism.³² Experimental data in comparison with simulations are shown in Fig. 6. The simulations yield a total film thickness of 22.7 nm and a surface and interface roughness of around 0.4 nm. We note that the X-ray reflectivity analysis was performed after the sample was exposed to air for longer time and therefore some oxide, present on the surface as discussed below, was included in the XRR simulations. For comparison with values determined by ellipsometry (see main text and the discussion in Sec. II below) we therefore use the total thickness. Given that different pieces of wafer were used for individual measurements (i.e. the same growth run but different storage conditions), we find an excellent agreement.

B. X-ray diffraction analysis of the tetragonal structure

Due to large penetration depth of x-ray photons, X-ray diffraction (XRD) probes the full film depth including the substrate below — the advantage being that no sample preparation is required for XRD measurements, which

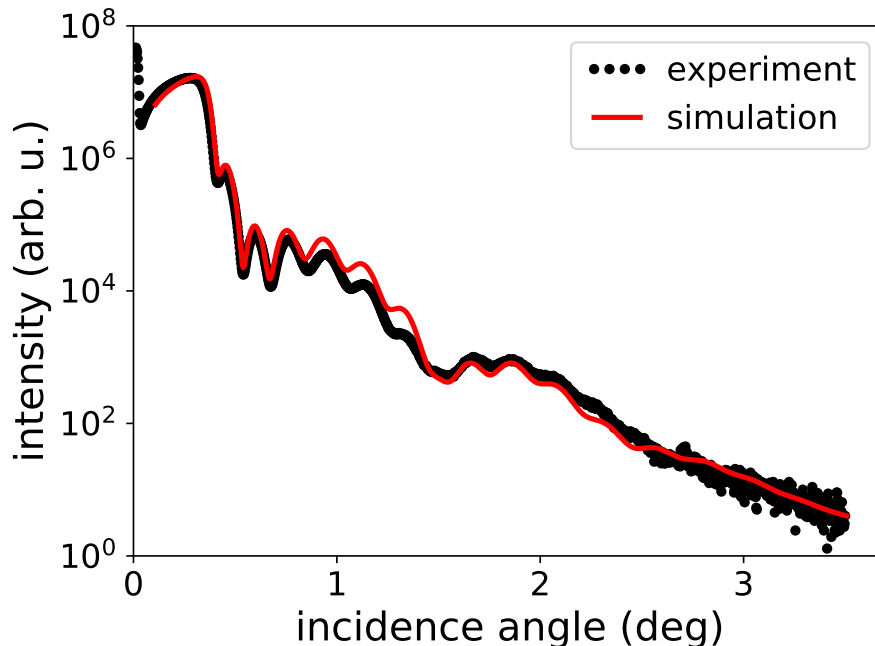


FIG. 6. X-ray reflectivity data and simulations of the sample investigated by ellipsometry.

description:	CuMnAs/GaAs	CuMnAs/GaP
	Ref. 31	this work
a [Å]	3.820(10)	3.853(1)
c [Å]	6.318(10)	6.276(1)
z/c for S^2	0.265(1)	0.259(1)
z/c for S^3	0.670(3)	0.664(1)
ADP [Å ²]	-	0.028(3)
R_B	-	3.97%

TABLE II. Structural parameters of CuMnAs thin films grown on GaP(001) and GaAs(001) substrates. The latter were converted from values published in Ref. 31.

therefore naturally complement the PEDT data in the main text. Despite certain other advantages, PEDT requires a complex specimen preparation. Further, XRD has a higher precision for lattice parameter measurements; thin films grown on GaP(001) yield lattice parameters specified in Tab. II. These measurements were performed using the aforementioned Rigaku Smartlab rotating anode system using monochromatic X-ray photons with $\text{CuK}_{\alpha 1}$ and a linear detector.

The determination of the atomic structure of the thin films was performed as described in detail in Ref. 31. For that purpose we used a Bruker D8-Discover diffractometer equipped with a Vantec-500 area detector. The difference between lattice parameter of CuMnAs (~ 6.3 Å) and GaP (~ 5.45 Å) warrants that no significant overlapping between diffraction peaks from substrate and from film takes place. The total number of diffraction peaks measured was 44. The number of observable diffractions is therefore considerably lower as in the PEDT data in the main text. This is compensated by easier modeling which in total only requires 5 structural parameters as opposed to observables (27 independent reflections) and a single one overall factor. The structural refinement includes an overall temperature factor, the two z/c positions of S_2 and S_3 , reported in the Tab. II. The shorter range in Q -space available for the long wavelength of Cu- $K\alpha$ (in comparison with electrons), hinders the refinement of individual temperature factors. Additionally, the relative electron densities of S_2 and S_3 positions (with respect to S_1) were refined. It can be appreciated that the values found are in a fairly good agreement with those in Tab. I in the main text.

II. SURFACE OXIDATION

Spectroscopic ellipsometry can be employed as an effective tool for the observation of time dependent changes on the sample surface which express themselves in surface optical properties that vary over time. Determination of optical constants relies heavily on the knowledge of sample's multilayer structure. Our thin layers of CuMnAs were exposed to air so that the presence of surface oxide layer may be expected. The following analysis led us to conclude that a few nanometres thick layer of cuprous oxide forms at a time scale of days. A freshly grown sample (20 nm thick CuMnAs layer on GaP) was put into the ellipsometer within two hours after being taken out from the MBE apparatus. A model structure assuming only the CuMnAs layer and surface roughness was used to fit experimental data as described in the main text resulting in the determination of optical parameters of CuMnAs.

Afterwards, the sample was exposed to air for about two weeks and the ellipsometric measurements were repeated several times during this time interval. The whole set of experimental data (i.e., for four different times of air exposure) was fitted at once with a modified model structure. This structure assumed another layer on top of CuMnAs. Only three thicknesses (l_{CuMnAs} , thickness of the additional layer l_o and surface roughness l_r) were left as fitting parameters. The best fit was obtained using optical parameters of Cu_2O and resulting thickness of this layer (l_o) was an increasing function of time elapsed from the growth. Manganese and arsenic oxides yielded clearly worse fits. Since the surface roughness in the fit was treated as an effective layer containing 50% of air and 50% of the oxide, the total effective thickness was calculated as $l_{\text{CuMnAs}} + l_o + \frac{1}{2}l_r$ and this quantity becomes larger in a matter of days, as shown in Fig. 7, and agrees very well (perhaps even surprisingly well) with the results of x-ray characterisation.

III. ORTHORHOMBIC SAMPLE

The imaginary part of permittivity shown by dashed line in Fig. 2 of the main text was measured on a bulk sample of CuMnAs grown using Bi flux similar to previously reported procedure^{38,39} for the growth of CuMn_3As_2 and $\text{Cu}_2\text{Mn}_4\text{As}_3$. The elements with starting molar ratio Cu:Mn:As:Bi was 1:1:1:10 (1:1:1:15 also gives good results) were

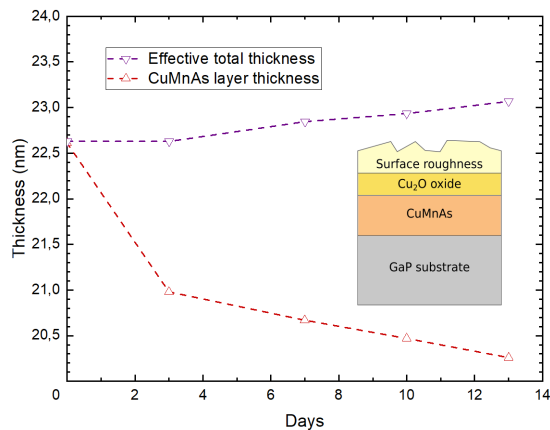


FIG. 7. After several days of air exposure (starting after the sample is taken out from MBE chamber), a thin oxide layer forms on the surface, gnawing at the actual material (CuMnAs). Nevertheless, the effective total thickness of the layer (see definition in the text) still slightly increases with time.

put into alumina crucibles (diameter 12 mm) and sealed under vacuum ($\sim 10^{-6}$ mbar) in quartz glass ampoules. The samples were slowly ($2^\circ/\text{min}$) heated up to 850°C and kept at fixed temperature for 10 h. Then, they were slowly cooled down to 400°C ($3^\circ\text{C}/\text{h}$) where the Bi flux was centrifuged. The single crystals were typically 1 to 3 mm long and 50 to $300\ \mu\text{m}$ thick with the mass under 0.5 mg. The composition of the prepared single crystals was determined using energy dispersive x-ray (EDX) analysis.

Single crystals with composition $\text{Cu}_{34}\text{Mn}_{33}\text{As}_{33}$ were then subject of further studies. The variation in composition in selected samples was under 0.5%. Ellipsometry was performed by the same procedure as for tetragonal films. The crystal symmetry and lattice parameters were determined by single crystal x-ray diffraction (XRD) using Rigaku RAPID II with Mo- $K\alpha$ radiation in transmission geometry. We have confirmed orthogonal structure (space group Pnma) with lattice parameters $a = 0.6598(4)$ nm, $b = 0.3861(4)$ nm and $c = 0.73015(1)$ nm. The lattice parameters and magnetic behaviour of prepared samples are in agreement with recently reported results on single crystals prepared by the same method.³⁹

Typical orthorhombic CuMnAs single crystal is shown in Fig. 8. The remaining Bi flux does not wet the surface and forms small droplets. For the ellipsometry measurements presented in this work, rather than etching and exposing the surface to water, we used fresh as grown surface and selected an area free of the bismuth droplets (focused beam with spot size 0.15 to 0.2 mm was used).

IV. UPS MODELLING AND IPES

In order to describe photoemission spectra, we used the so called one-step model of photoemission. We used recently developed fully spin-density matrix formulation for the photocurrent³⁴ within the relativistic KorringaKohnRostoker (SPR-KKR) Green function method. As a first step of our PES investigations, we performed self-consistent LSDA+U ground state calculations for CuMnAs by means of SPR-KKR method. All parameters of the calculations has been as far as possible same as for the above mentioned LAPW based investigations and results obtained within SPR-KKR method are quantitatively comparable to the LAPW method. The self consistent potentials and LSDA+U self energy are then used as an input for UPS and IPE investigations of CuMnAs(001) surface. As the LSDA+U does not include many-body finite life-time of the initial state this effect was included phenomenologically by imaginary part of potential (0.05 eV). The impurity scattering of the final state and its inelastic mean free path was modelled again by the imaginary part of the inner potential (2.0 eV) as usual.³³

Additionally, for the photoemission calculations, we accounted for the surface barrier by use of a Rundgren-Malmström surface potential³⁵, which is included as an additional layer. This procedure is described in for example in Ref. 36 and it accounts for the energetics and dispersion of all surface features. One of the most important parameters for this surface potential is the position of the classical image plane which in other words describes distance between surface barrier and last surface layer. In the left panel of Fig. 9, we show UPS spectra calculated for the position of the image plane in the range between $0.14c$ and $0.32c$. The spectral feature close to the Fermi level (B in Fig. 5 of the main text) clearly shows a strong surface character. On the other hand, the main peak at binding energy of -4 eV (feature A of Fig. 5) are bulk states with predominant Mn-character.

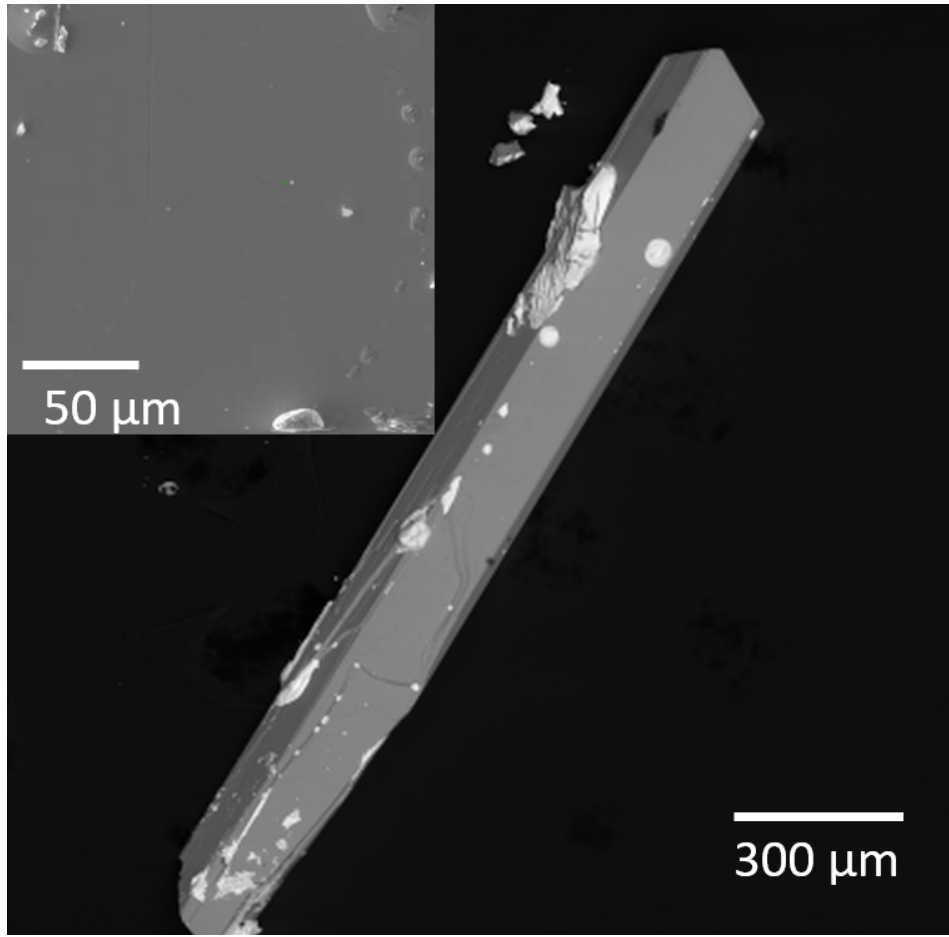


FIG. 8. Image of orthorhombic CuMnAs single crystals taken by SEM microscope. In BSE contrast, the remaining Bi flux droplets are bright and clearly visible. The inset shows detail (SE contrast) on the sample surface with a clean area suitable for ellipsometric measurements.

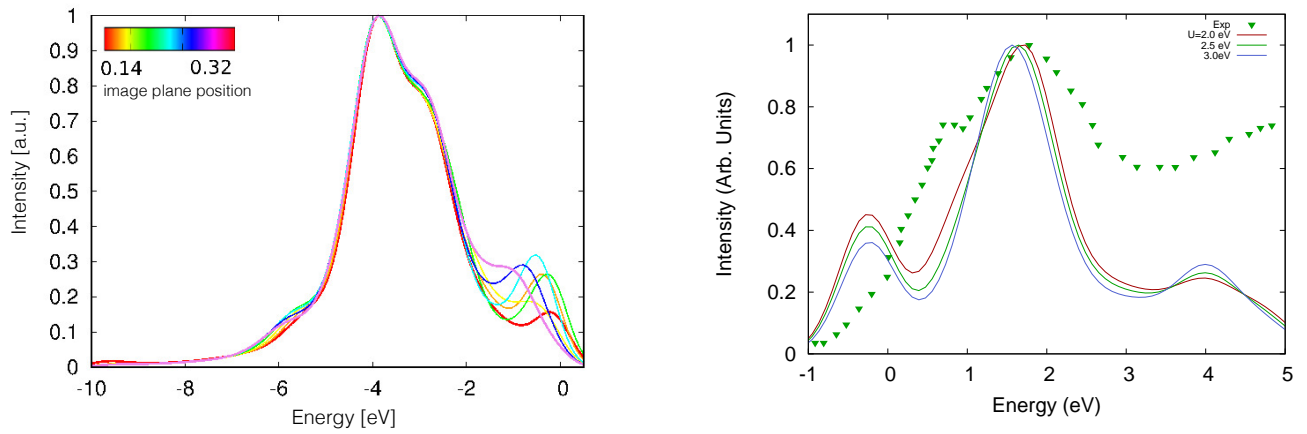


FIG. 9. *Left*: Result of one-step model of UPS ($U = 3$ eV) for different models of the surface barrier. *Right*: IPES measurement and modelling (RTP).

The conduction band electronic structure of the interfaces was studied by means of Inverse PhotoEmission Spectroscopy (IPES). Spectrum after integral background subtraction³⁷ is shown in the right panel of Fig. 9. The apparatus consists of an electron source based on a negative electron affinity GaAs photocathode coupled to an appropriate transport electron optics and a bandpass out-coming photons detector at fixed energy (9.3 eV) employing a KBr photocathode and a SrF₂ window. Like in the case of UPS, the Gaussian instrumental resolution broadening has been taken into account with FWHM = 0.8 eV (a conservative estimate³⁷), evaluated measuring the IPES Fermi-edge of a monocrystalline Ag sample. In this case, the instrumental broadening is so high that it has not been necessary to consider the energy spreading due to lifetime effects. Agreement between experimental data and one-step model of photoemission is good, again there is one dominant peak (close to energy of 2 eV) which matches well the calculations whose dependence on Hubbard U is weaker than in the case of UPS. Spectral features below the energy of 1 eV are related to surface states.
